5-2015

Development of Pyrolysis Models for Charring Polymers

Jing Li
University of New Haven, jli@newhaven.edu

Junhui Gong
Nanjing University of Information Science and Technology

Stanislav I. Stoliarov
University of Maryland - College Park

Publisher Citation

Li, J., J. Gong and S. I. Stoliarov (2015). "Development of pyrolysis models for charring polymers." Polymer Degradation and Stability, Volume 115, May 2015, Pages 138-152.

Comments

This is the author's accepted version of the article published in Polymer Degradation and Stability. The final version can be accessed via http://dx.doi.org/10.1016/j.polymdegradstab.2015.03.003

Development of Pyrolysis Models for Charring Polymers

Jing Li[a,b], Junhui Gong[c] and Stanislav I. Stoliarov*[,a]

[a]University of Maryland, Department of Fire Protection Engineering, College Park, MD 20742, United States

[b]University of New Haven, Department of Fire Science, West Haven, CT 06516, United States

[c]Nanjing University of Technology, College of Urban Construction and Safety Engineering, Nanjing 210009, China

Accepted by PDST (http://www.sciencedirect.com/science/article/pii/S0141391015000671)

Abstract

Controlled atmosphere, radiation-driven gasification experiments were conducted on a series of synthetic polymers including poly(acrylonitrile butadiene styrene), poly(ethylene terephthalate), poly(methyl methacrylate)-poly(vinyl chloride) alloy (Kydex) and polyetherimide. Mass loss rate and non-radiated surface temperature of coupon-sized material samples were measured simultaneously and recorded as a function of time. These temperature data were combined with the results of broadband radiation absorption measurements and previously conducted thermogravimetric analysis (TGA) and differential scanning calorimetry (DSC) to characterize the transport of thermal energy inside the gasifying materials through inverse modeling. Subsequently, complete pyrolysis models, based on the kinetics and thermodynamics of the thermal decomposition derived from the TGA and DSC experiments, were formulated and employed to predict the mass loss rate histories obtained at 30-90 kW m^{-2} of external radiant heat flux simulating fire exposure. Satisfactory predictions were obtained for all materials with the exception of polyetherimide, which highly intumescent behavior introduced large uncertainties in the gasification conditions.

Keywords: *polymer flammability; burning rate; thermophysical properties; intumescence; ThermaKin*

*Corresponding author. E-mail: stolia@umd.edu

1. Introduction

It is widely recognized that charring polymers, materials that form solid, thermally stable and oxidation resistant residue upon thermal decomposition, tend to have lower flammability than non-charring polymers. One of the main strategies to improve flame resistance of a polymeric solid is to alter its molecular structure or compound it with chemicals that increase its propensity to char [1]. Polymer flammability can be generally characterized by the evolution of the rate of gaseous fuel production (or mass loss rate) in response to application of a radiative or convective heat flux to a defined area of the material sample. Multiplication of this rate by the effective heat of combustion of the gaseous fuel yields heat release rate, which is the single most important parameter describing dynamics of fire growth [2].

A significant benefit can be derived from a capability to simulate pyrolysis of charring polymers in order to predict their mass loss rate. Such simulations, if accurate, enable fast and effortless evaluation of material flammability in a wide range of fire scenarios and may offer critical insights into optimization of the material's composition and structure to achieve better performance. Atreya [3], Di Blasi [4], Moghtaderi [5], Staggs [6] and Delichatsios [7], among others, developed essential mathematics of continuum pyrolysis models for charring materials and proposed approaches to their parameterization. It should be noted that the majority of their effort has been focused on lignocellulosic materials.

Our group has recently developed a method, based on carefully calibrated milligram-scale thermal analysis experiments, that provides a comprehensive characterization of the kinetics and thermodynamics of the thermal decomposition for non-charring [8] as well as charring polymers [9]. This method yields a set of parameters including semi-global decomposition reaction kinetics, heat capacities, heat of melting and heats of decomposition reactions, which represents the core of the input required for the state-of-the-art pyrolysis models [10-12]. In the current study, these parameters were combined, through modeling, with the results of simple infrared radiation absorption measurements and new gram-scale gasification experiments utilizing simultaneous sample mass and temperature monitoring to produce fully parameterized pyrolysis models. The absorption measurements were used to define radiative heat transport through the unpyrolyzed materials, while the gasification temperature measurements provided the information necessary to compute the condensed-phase thermal

conductivities as a function of temperature and local composition. The mass loss rate histories obtained from the gasification experiments were employed to validate these pyrolysis models.

This approach to pyrolysis model parameterization has already been demonstrated to provide accurate mass loss rate predictions for non-charring polymers [13]. In the current work, an applicability of this approach to charring polymers including poly(acrylonitrile butadiene styrene) (ABS), poly(ethylene terephthalate) (PET), poly(methyl methacrylate)-poly(vinyl chloride) alloy (Kydex) and polyetherimide (PEI) was examined. These materials are listed in the order of increasing char yield with ABS being essentially non-charring (< 3 wt.% char yield) and PEI having the highest char yield (≈50 wt.%). ABS was included into this study because, as the subsequent analysis shows, its char still produces a thermally insulating layer, which impact on the material's mass loss rate cannot be neglected.

2. Materials and Methods

2.1 Materials

ABS, PET, Kydex and PEI were purchased in a form of large (approximately 1.2×0.6 m), extruded sheets. These sheets were 6.4, 6.7, 6.1 and 6.6 mm thick, respectively. Detailed information on the source of purchased materials is provided in Table 1. The density of these materials was measured at room temperature (≈300 K) and found to be 1050, 1385, 1350 and 1285 kg m^{-3}, respectively. To minimize variation in the moisture content, all material samples were stored in a desiccator in the presence of Drierite for a minimum of 48 hours prior to testing.

Table 1. Source of materials studied in this work.

Polymer	Manufacturer	Trade Name	Distributor
Poly(acrylonitrile butadiene styrene) (ABS)	Westlake Plastics	Absylux	Modern Plastics
Poly(ethylene terephthalate) (PET)	Ensinger	PET	Curbell Plastics
Poly(methyl methacrylate)-poly(vinyl chloride) alloy (Kydex)	Kydex, LLC	Kydex T	Professional Plastics
Polyetherimide (PEI)	GE Plastics	Ultem 1000	Curbell Plastics

2.2 Thermal Analysis Experiments

4-7 mg, thin-film samples were cut from the extruded sheets and subjected to a linear heating at a rate of 10 K min^{-1} in a nitrogen atmosphere using a simultaneous thermal analyzer, Netzsch F3 Jupiter, capable of thermogravimetric analysis and differential scanning calorimetry. Sample mass and heat flow into these samples were recorded as a function of time and temperature and a numerical analysis was conducted to derive both kinetics and thermodynamics of the material's thermal decomposition. A detailed description of these experiments and analysis is provided elsewhere [8-9].

2.3 Gasification Experiments

80×80 mm square plates were cut from the extruded sheets and gasified using controlled radiant heating. These experiments were performed in a Govmark CC-1 cone calorimeter [14] equipped with the Controlled Atmosphere Pyrolysis Apparatus (CAPA) [15]. The cone calorimeter radiant heater was employed to deliver a steady heat flux to the top surface of a horizontally mounted sample. This surface was initially located 40 mm below the bottom of the heater. The calorimeter's precision balance was used to monitor the sample's mass loss. The calorimeter's exhaust system, which was operated at 1440 L min^{-1}, was used to remove gaseous pyrolysis products.

The CAPA, which was operated at 225 standard L min^{-1} of nitrogen, was used to create a near anaerobic environment, oxygen concentration <3 vol.%, in the vicinity of the sample. The oxygen concentration was measured by sampling from the atmosphere above the initial position of the top sample surface and analyzing this atmosphere with Servomex 4100 gas analyzer. Anaerobic conditions were used in both thermal analysis and gasification experiments to simulate material degradation under a laminar flame sheet. It should be noted that, during the experiments on Kydex and PEI, significant changes in the pyrolyzing sample size and shape made it impossible to control oxygen concentration at the sample surface for the full duration of these experiments. Both materials demonstrated highly intumescent behavior; their samples expanded outside of the CAPA boundaries and into the cone heater (oxygen concentration >10 vol.%) late in the gasification process. These factors were taken into account during subsequent analysis of the experimental data.

The CAPA was modified to add additional diagnostics. A schematic of the modified CAPA is shown in Figure 1. A portion of the CAPA's external wall was replaced with a quartz plate to enable videotaping of the changes in the sample's geometry during gasification. The CAPA's sample holder was redesigned to provide an optical access to the bottom sample surface. The sample was placed on a 0.8 mm thick aluminum mesh. For materials that demonstrated significant melt flow, ABS and PET, a layer of 0.03 mm thick aluminum foil was placed between the sample bottom and the mesh to prevent dripping through the mesh. The perimeter of each sample was wrapped with a 0.1 mm thick paper tape and thermally insulated with a 5 mm wide strip of Kaowool PM.

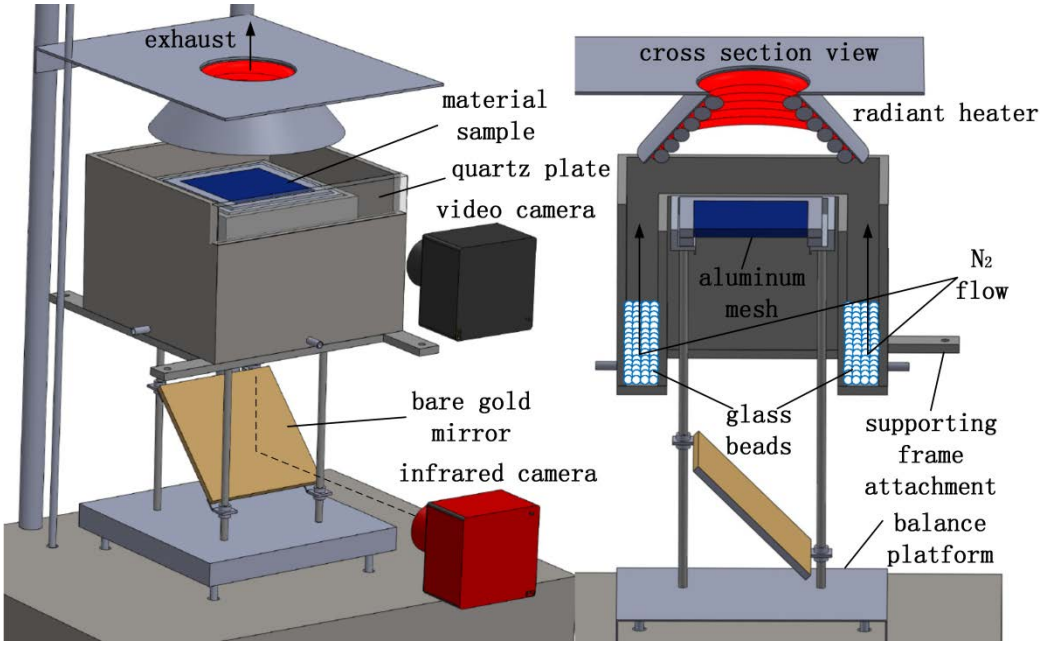

Figure 1. Schematic of the modified Controlled Atmosphere Pyrolysis Apparatus.

A temperature-calibrated infrared camera, FLIR E40, was focused on the bottom sample surface through a gold-coated flat mirror (0.97 reflectivity in 0.8-10 μm range). A coat of high emissivity, 0.95, paint was applied to the sample, aluminum mesh and foil surfaces facing the camera to ensure correct temperature reading and provide well-defined thermal conditions at this boundary. The temperature readings were taken through the spacing in the aluminum mesh,

which covered only about 20% of the bottom sample surface. The validity of this approach to sample surface temperature measurement was examined and verified in previous studies [13,16].

The experiments were performed at 30, 50 and 70 kW m^{-2} of set radiant heat flux for all materials with the exception of PEI, which was studied at 50, 70 and 90 kW m^{-2} because of its exceptional thermal stability. The data from the PET experiments conducted at 30 kW m^{-2} were compromised by intense dripping and spattering of the pyrolyzing material and were excluded from further consideration. The heat fluxes were set using a water-cooled Schmidt-Boelter heat flux gauge, which was positioned at a location corresponding to the geometric center of the initial position of the top sample surface. 30 kW m^{-2} heat flux corresponded to the heater temperature of about 915 K. 90 kW m^{-2} heat flux corresponded to the heater temperature of about 1200 K.

Spatial variation in this heat flux was examined in an attempt to account for the changes in the heating conditions experienced by expanding samples. It was determined that, for the first 20 mm above the initial position of the top sample surface, the heat flux increased by about 0.9% per 1 mm decrease in the distance to the bottom of the heater. The heat flux was also found to be essentially uniform within 80×80 mm horizontal planes (within 5-7% of the center reading).

Convective losses from the top and bottom surfaces of the CAPA samples were characterized [13,15] and further validated [16] in previous studies. The top surface losses were found to be well represented by a convection coefficient of 5 W m^{-2} K^{-1} and background gas temperature that changed linearly from 340 to 400 K as the radiant heat flux increased from 30 to 90 kW m^{-2}. The bottom surface losses were found to be well represented by a convection coefficient of 4 W m^{-2} K^{-1} and constant background temperature of 310 K. It was assumed that pyrolysis-induced changes in the sample geometry, which were significant in the case of Kydex and PEI, did not alter the dynamics of convective cooling of the sample's top surfaces.

Each gasification experiment (at a given set of conditions) was repeated 3 times to accumulate statistics. Sample mass data were collected at a frequency of 1 Hz and differentiated numerically using 4 s time intervals to compute mass loss rate. The infrared camera temperature maps of the bottom sample surface were collected at a frequency of 7.5 Hz. To examine potential non-uniformity of the temperature of the surface, it was subdivided into 3 regions as shown in Figure 2. Thirty six pixels were randomly selected from each region to compute its

mean temperature. The computed mass loss rate and region-specific mean temperature histories were further averaged over the three gasification experiments.

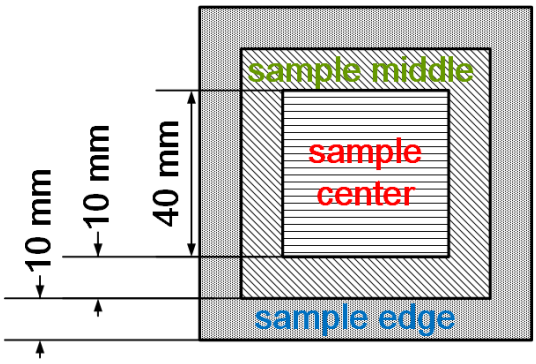

Figure 2. Bottom sample surface regions whose mean temperatures were determined and analyzed in this study.

2.4 Radiation Absorption Measurements

The broadband infrared absorption coefficients of unpyrolyzed materials were estimated by placing 1.5 mm thick film samples between the cone calorimeter radiant heater and a water-cooled Schmidt-Boelter heat flux gauge and determining the fraction of radiation transmitted through these films. The films, which were machined from the extruded sheets, were exposed to 35 kW m^{-2} of incident radiant heat. To avoid contributions associated with conduction through the sample, the data on transmitted radiation were collected for the first 5 s after the beginning of exposure. These measurements were repeated twice for each material. Details of the experimental setup are outlined in a previous publication [13]. This setup and procedure were based on an earlier work by Linteris et al. [17].

The radiative transport was assumed to be one-dimensional and insensitive to the variation in the spectral characteristics of the cone heater with set heat flux. A Beer-Lambert-law-based expression taking into account radiation reflection at the polymer-air interfaces, which was previously utilized by Tsilingiris [18], was used to compute the absorption coefficients from the data on transmitted radiation. Broadband surface reflectivity of all polymers was estimated

to be 0.05. This reflectivity value was computed from the index of refraction, which shows little variation among thermoplastics [17].

2.5 Modeling

The ThermaKin numerical modeling environment was employed to analyze the gasification temperature data and to construct pyrolysis models to predict the rate of mass loss observed in the gasification experiments. ThermaKin solves non-steady energy and mass conservation equations for chemical reactions between material components. Each material component specified in the model is characterized by a set of temperature dependent properties that define heat transfer and mass transport through the condensed phase. ThermaKin can be used to conduct one-dimensional or two-dimensional simulations. Only one-dimensional simulations, consistent with the initial conditions realized in the gasification experiments, were performed in this study despite the fact that notable deviations from these conditions were observed at late stages of gasification of Kydex and PEI, as discussed in the next section.

The key governing equations of the one-dimensional ThermaKin are summarized as follows:

$$\frac{\partial \xi_j}{\partial t} = \sum_{i=1}^{Nr} \theta_i^j r_i - \frac{\partial J_j}{\partial x} + \frac{\partial}{\partial x}\left(\xi_j \int_0^x \frac{1}{\rho}\frac{\partial \rho}{\partial t} dx \right) \qquad (1)$$

$$\sum_{j=1}^{N} \xi_j c_j \frac{\partial T}{\partial t} = -\sum_{i=1}^{Nr} h_i r_i - \frac{\partial q}{\partial x} - \frac{\partial I_{ex}}{\partial x} + \frac{\partial I_{rr}}{\partial x} - \sum_{g=1}^{N_g} c_g J_g \frac{\partial T}{\partial x} + c\rho \frac{\partial T}{\partial x} \int_0^x \frac{1}{\rho}\frac{\partial \rho}{\partial t} dx \qquad (2)$$

$$r_i = A_i \exp\left(-\frac{E_i}{RT} \right) \xi_k \, \xi_l \quad (3); \qquad J_g = -\rho_g \lambda \frac{\partial \left(\xi_g / \rho_g \right)}{\partial x} \quad (4); \qquad q = -k \frac{\partial T}{\partial x} \quad (5)$$

$$\frac{\partial I_{ex}}{\partial x} = -I_{ex} \sum_{j=1}^{N} \alpha_j \xi_j \quad (6); \qquad \frac{\partial I_{rr}}{\partial x} = \frac{\varepsilon \sigma T^4}{I_{ex}^0} \frac{\partial I_{ex}}{\partial x} \quad (7)$$

Equation 1 is component *j* mass conservation statement formulated in terms of this component's concentration, ξ_j. This statement accounts for component consumption/production in chemical reactions, the rate of which is defined by Equation 3, gas flow within the solid, the flux of which is defined by Equation 4, and mass transfer associated with contraction/expansion of the material object (the last term in Equation 1). Equation 2 is the energy balance formulated in terms of

temperature, T. This balance includes heat produced in chemical reactions, heat transfer due to conduction, the flux of which is given by Equation 5, radiative heat from an external source, the absorption of which is defined by Equation 6, re-radiation of energy to the environment defined by Equation 7, and convection associated with gaseous component flow (the fifth right-hand-side term in Equation 2) and overall material expansion/contraction (the last term in Equation 2).

The symbols in Equations 1-7 are defined as follows. t is time; θ is a stoichiometric coefficient, which is negative when the corresponding component is a reactant and positive when it is a product; x is the Cartesian coordinate. ρ and c are density and heat capacity. h is the heat of reaction; A and E are the Arrhenius parameters; and R is the molar gas constant. λ, k and α are gas transfer, thermal conductivity, and radiation absorption coefficients. ε is the broadband emissivity; σ is the Stefan-Boltzmann constant; and I_{ex}^{0} is the external radiation through an object boundary (incident radiation minus reflected).

Properties without a subscript indicate the property of mixture (rather than that of an individual component). The density of mixture is defined as one over the sum of component mass fractions divided by the corresponding component densities. The volumetric contribution of gaseous components can be scaled by a user defined factor related to the local composition. In the current simulations, this factor was set to 0. Intumescence was modeled by assigning lower densities to the material components representing solid decomposition products, as explained in the next section. A detailed description of the ThermaKin physics and numerical solution methodology can be found in previous publications [10,19].

The mass transport and convective and radiative heat transfer boundary conditions were defined at the top and bottom surfaces of the computational domain to represent the corresponding conditions of the simulated experiment (these conditions are reported in Subsection 2.3 and further discussed in the next section). The top surface was assumed to provide no resistance to gas flow, while the bottom surface was set to be impenetrable to gases. The gas transport coefficient was set sufficiently high, 2×10^{-5} m^2 s^{-1}, for all components in the simulations to ensure that the fluxes of gases out of the top surface were always equal to their rates of production inside the material and the concentrations of gases inside the material were negligible. The heat capacity of all gaseous decomposition products was assumed to be equal to 1.8 kJ kg^{-1} K^{-1}, which was the mean heat capacity of a series of C1-C8 hydrocarbons at 400-500

K [20]. The value of heat capacity had a minor impact on the simulation results because of the fast transport assumption implemented in the model. All calculations were performed using 0.025 mm spatial discretization and 0.005 s time step. Increasing or decreasing these integration parameters by a factor of 2 did not produce any significant changes in the results of the simulations indicating convergence of the numerical solutions.

3. Results and Discussion

3.1 Kinetics and Thermodynamics of Thermal Decomposition

The polymer decomposition kinetics and thermodynamics obtained from the simultaneous thermal analysis experiments are summarized in Table 2 and 3. The decomposition of ABS was represented by a single first order reaction (the concentration of the second, *l*'s, component in Equation 3 was set to unity), while the decomposition of PET, Kydex and PEI was represented by two consecutive first order reactions. Each of these reactions had one condensed-phase and one gaseous product. The intermediate condensed-phase product of PET, Kydex and PEI was labeled as PET_int, Kydex_int and PEI_int, respectively. The final condensed-phase product for ABS, PET, Kydex and PEI was labeled as ABS_char, PET_char, Kydex_char and PEI_char, respectively. The Arrhenius parameters (A and E) and the condensed-phase product yield (θ) of each reaction are listed in Table 2. The heats of reaction (h) are listed in Table 3 (endo is positive). The numerical subscripts refer to the first or second (consecutive) reaction. Note that these reactions describe a semi-global decomposition mechanism formulated to capture key features of the thermal analysis mass loss dynamics and corresponding heat flow.

A first order reaction was also used to represent melting of PET and PEI. This reaction had only one product, PET_melt and PEI_melt, respectively. The reaction was specified to turn on at the measured melting point and occur with a temperature independent rate constant of 1 s^{-1}. The melting points and heats (T_m and h_m) are listed in Table 3.

The heat capacities of the polymers and their condensed-phase decomposition products were also obtained from the thermal analysis experiments. These heat capacities were represented by linear temperature dependencies, which are listed in Table 3. The heat capacity of ABS_char could not be measured because of its small yield (< 3 wt.%) and was assumed to be equal to that of PET_char.

Table 2. Kinetic parameters describing polymer decomposition [8-9].

Polymer	A_1 (s^{-1})	E_1 (kJ mol^{-1})	θ_1	A_2 (s^{-1})	E_2 (kJ mol^{-1})	θ_2
ABS	1.00×10^{14} ±40%	219 ±2%	0.02	N/A	N/A	N/A
PET	1.60×10^{15} ±30%	235 ±8%	0.18	3.53×10^{4} ±30%	96 ±10%	0.72
Kydex	6.03×10^{10} ±50%	141 ±3%	0.45	1.36×10^{10} ±40%	174 ±5%	0.31
PEI	7.66×10^{27} ±50%	465 ±7%	0.65	6.50×10^{2} ±50%	88 ±10%	0.77

Table 3. Thermodynamic parameters describing polymer melting and decomposition [8-9]. Endo is positive.

Polymer	Heat Capacity (kJ kg^{-1} K^{-1})	T_m (K)	h_m (kJ kg^{-1})	h_1 (kJ kg^{-1})	h_2 (kJ kg^{-1})
ABS	ABS: $(1.58+1.30\times10^{-3}T)$ ±22% ABS_char: $(0.82+1.12\times10^{-4}T)$ ±10%	N/A	N/A	460 ± 5%	N/A
PET	PET: $(-0.27+4.64\times10^{-3}T)$ ±12% PET_melt: $(2.05-2.08\times10^{-4}T)$ ±15% PET_int: $(1.44-4.8\times10^{-5}T)$ ±13% PET_char: $(0.82+1.12\times10^{-4}T)$ ±10%	525	30 ±10%	220 ±7%	250 ±25%
Kydex	Kydex: $(-0.62+5.93\times10^{-3}T)$ ±8% Kydex_int: $(0.27+3.01\times10^{-3}T)$ ±12% Kydex_char: $(1.15+9.6\times10^{-5}T)$ ±15%	N/A	N/A	180 ±10%	125 ±12%
PEI	PEI: $(-0.04+4.11\times10^{-3}T)$ ±16% PEI_melt: $(1.88+5.75\times10^{-4}T)$ ±20% PEI_int: $(1.59+3.08\times10^{-4}T)$ ±14% PEI_char: $(1.30+4.1\times10^{-5}T)$ ±8%	500	1 ±150%	-80 ±15%	-5 ±200%

3.2 Gasification Experiments – General Observations

A series of time-stamped snapshots of the gasification experiments conducted at 50 kW m^{-2} of external heat flux is shown in Figure 3, 4, 5 and 6. The top images (within each snapshot) are single frames from a digital video camera, which provide a sideview of the gasifying sample. The bottom images are temperature maps of the bottom sample surfaces (taken at the same time).

ABS samples (Figure 3) showed no significant swelling during pyrolysis. PET samples (Figure 4) swelled somewhat, while retaining essentially rectangular cross section throughout the process. Kydex samples (Figure 5) grew in height more significantly. They maintained approximately rectangular shape for the first 200 s of the gasification. Subsequently, this shape gradually transitioned to a pyramid-like structure with the tip of the pyramid representing the bottom of the sample. This transition is reflected on the temperature maps, which show a continuous reduction in the surface area of the sample's base (note that a crescent-like shape on the Kydex temperature maps is a shadow of the cone heater mount). PEI samples (Figure 6) grew in height even faster than Kydex samples. These samples assumed pyramid-like shape, with the tip facing upward, early in the gasification process and maintained this shape throughout. The top of the PEI samples reached deep inside the cone heater at the late stages of the gasification.

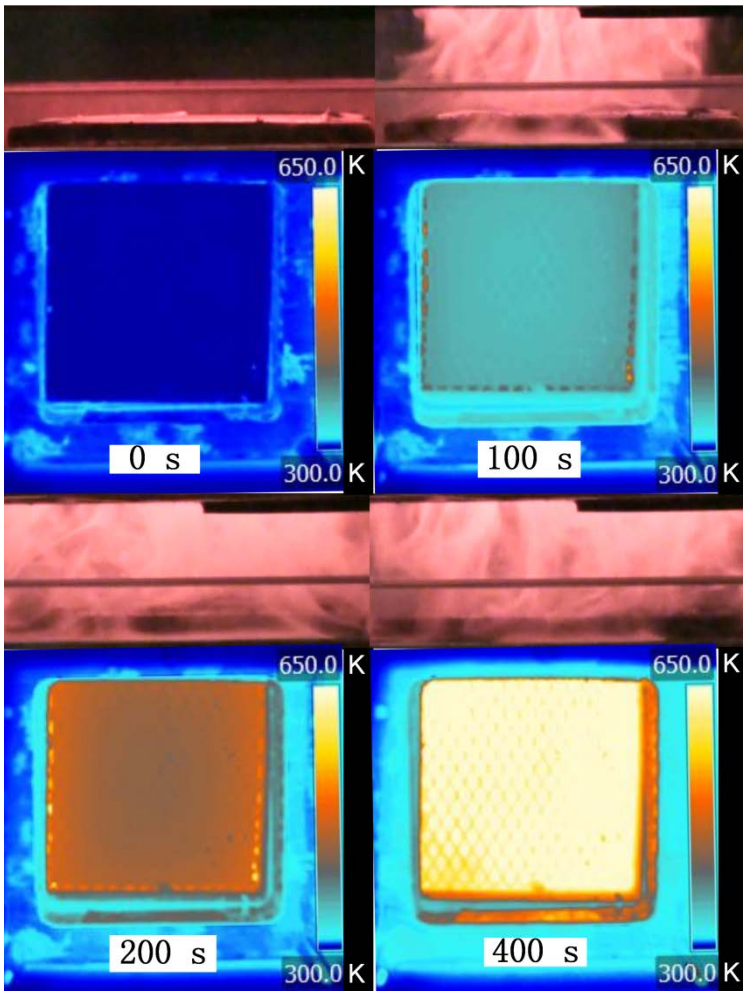

Figure 3. Sideview images and bottom surface temperature maps of ABS sample being gasified in CAPA at 50 kW m^{-2} of external heat flux.

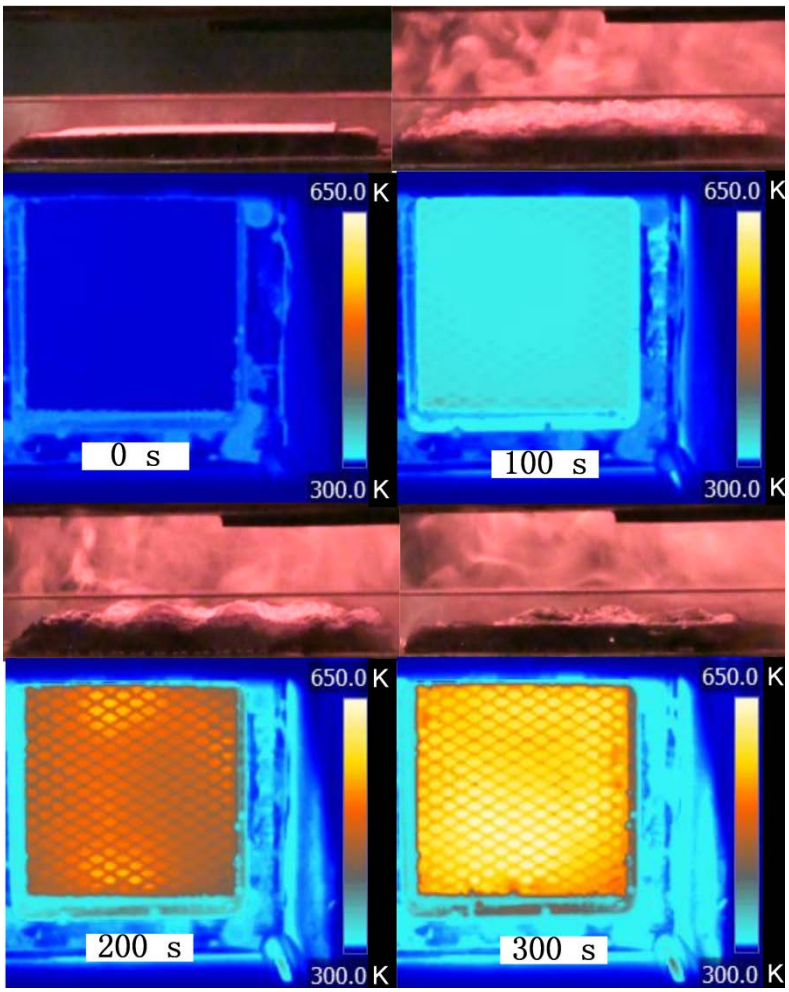

Figure 4. Sideview images and bottom surface temperature maps of PET sample being gasified in CAPA at 50 kW m^{-2} of external heat flux.

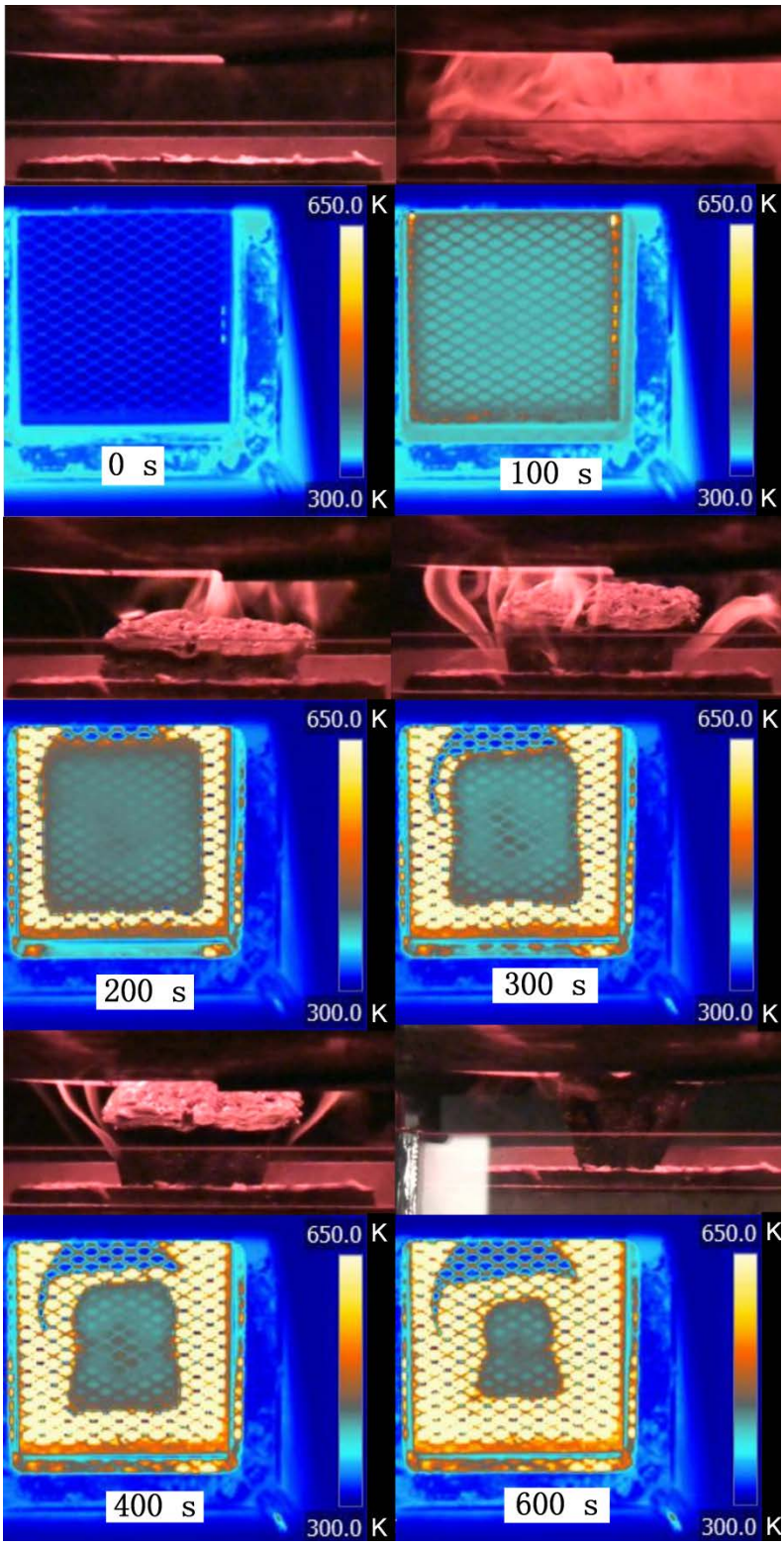

Figure 5. Sideview images and bottom surface temperature maps of Kydex sample being gasified in CAPA at 50 kW m^{-2} of external heat flux.

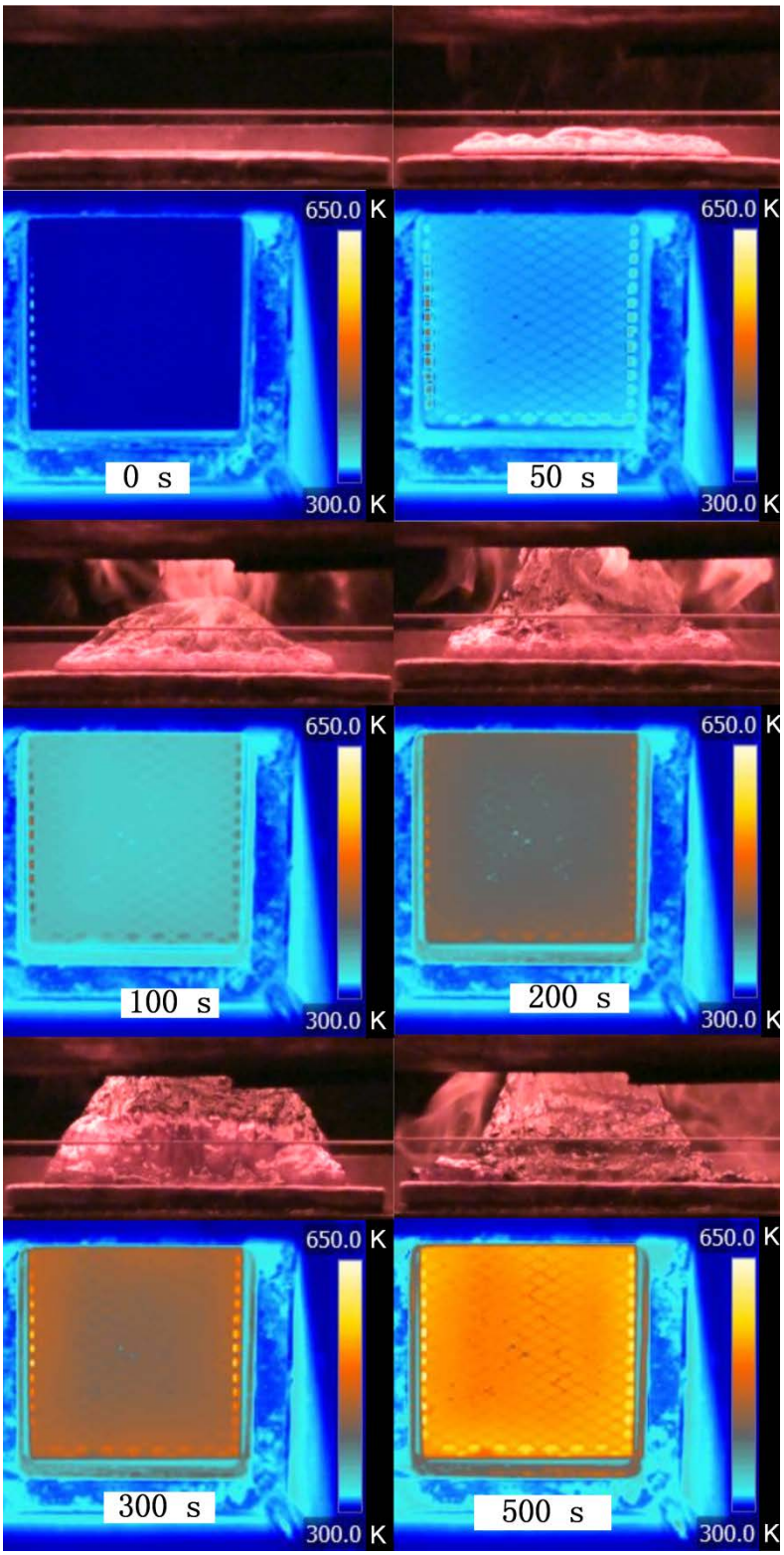

Figure 6. Sideview images and bottom surface temperature maps of PEI sample being gasified in CAPA at 50 kW m^{-2} of external heat flux.

To account for the changes in the radiative heat flux incident on the top surfaces of Kydex and PEI, the position of these surfaces was estimated from the sideview video. For Kydex, this position was defined by the distance between the highest visible point of the surface and the sample bottom. For PEI, 80% of such distance was used to provide a somewhat arbitrary correction for the pyramid-like shape of the pyrolyzing sample. The distance information could only be collected while the top of the sample was not obscured by the body of the cone heater. These distances (or sample thicknesses) are plotted as points with respect to time in Figure 7 for all gasification tests performed on these materials. The uncertainties, shown as error bars, were calculated as two standard deviations of the mean. This approach to reporting uncertainties is employed throughout the manuscript.

These distance dependencies on time were approximated by linear functions, which are depicted as lines in Figure 7, and converted to the heat flux dependencies on time shown in Figure 8. This conversion was based on a measurement (described in Subsection 2.3) that indicated that the heat flux increases by 0.9% per 1 mm decrease in the distance to the cone heater. It was assumed that, after the top sample surfaces reach 24 mm above their initial positions, the heat flux stops increasing and remains steady for the rest of the gasification experiment. These incident radiative heat flux trends were implemented as time dependent boundary conditions in the simulations discussed in the following subsections.

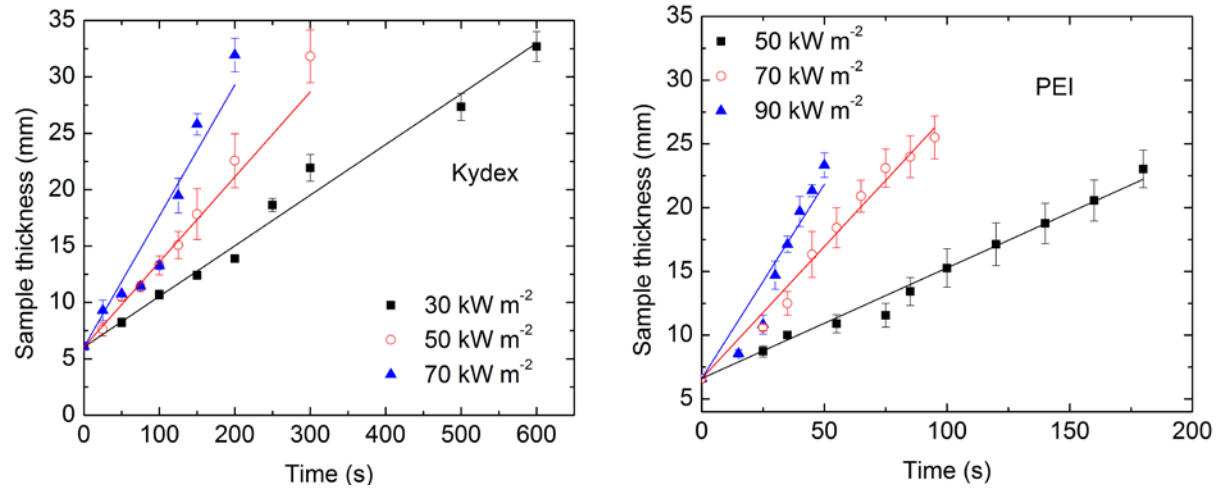

Figure 7. Sample swelling dynamics observed in the gasification experiments. The lines are linear fits of the data shown as points.

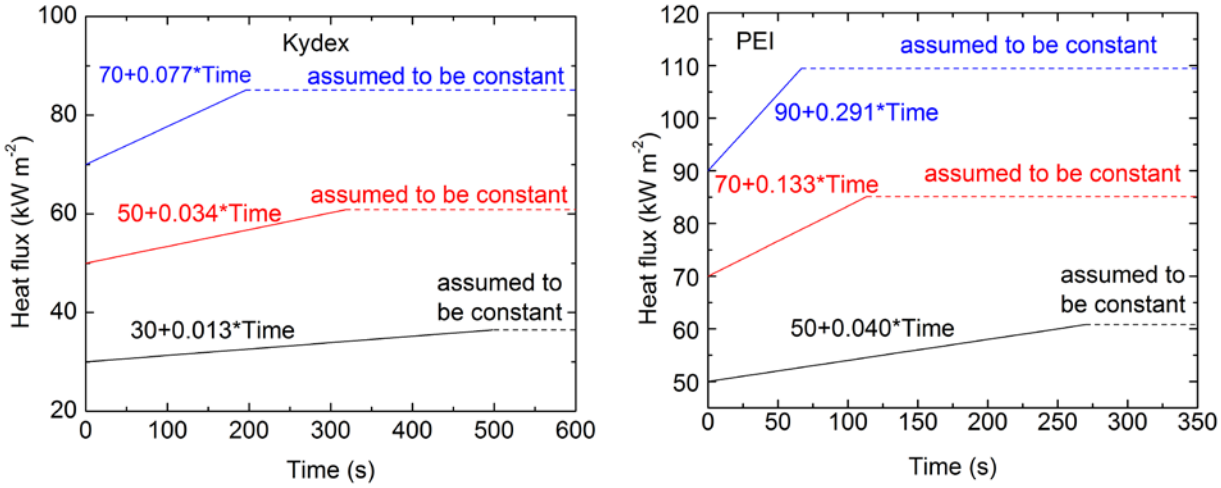

Figure 8. Radiative heat flux incident onto the top surface of samples showing significant swelling during gasification.

The sample residues remaining after the completion of the 50 kW m^{-2} gasification experiments were carefully removed from the CAPA and cooled down to room temperature. Their bulk densities were subsequently computed from their mass and volume, which was estimated by approximating the shape of the residue by that of a rectangular prism (for PET) or square pyramid (for Kydex and PEI). This density values were assigned to the final condensed-

phase products of these materials. The density of PET_char, Kydex_char and PEI_char were specified to be 80, 100 and 80 kg m^{-3}, respectively. The density of ABS residue could not be determined due to its negligible amount. Therefore, the density of ABS_char was assumed to be equal to the density of PET_char. A more detailed description of this residue density analysis can be found elsewhere [16].

3.3 Heat Transfer in Gasifying Materials

The polymer broadband absorption coefficients were computed using the data from the infrared radiation transmission experiments and normalized by density (used as a surrogate for concentration). The mean coefficient values were found to be 1.71, 1.40, 1.58 and 1.36 m^2 kg^{-1} for ABS, PET, Kydex and PEI, respectively. These values were found to vary by less than 5% between the two consecutive measurements. It should be noted that, in addition to being a function of the spectral characteristics of the incident infrared radiation, these coefficients depend on the thickness of material sample used in the measurement [17]. However, as long as the measured values indicate that most of the radiation is absorbed within a relatively small (<0.5 mm) depth, as is the case here, the impact of ignoring this dependence on the overall heat transfer is expected to be negligible.

The measured absorption coefficients were assigned to the material components representing the corresponding unpyrolyzed materials. The components representing the final condensed-phase products of decomposition were assumed to be effectively non-transparent to radiation; their absorption coefficient was set at 100 m^2 kg^{-1}. The exception was ABS_char, which absorption coefficient was used as an adjustable parameter during the gasification heat transfer modeling. For the rest of the condensed-phase material components (representing molten or partially degraded polymers), the absorption coefficient was selected to be equal to either that of the unpyrolyzed material, final condensed-phase product, or the mean of the two values. As in the case of ABS_char, these selections were made during the gasification heat transfer modeling described later in this subsection.

The emissivity of all material components, with the exception of those representing the final condensed-phase products of decomposition, was set at 0.95, one minus the reflectivity of unpyrolyzed polymers. Based on apparent high carbon content of all gasification residues, the emissivity of the final condensed-phase products was assigned the emissivity of graphite, 0.86

[21]. The material components representing unpyrolyzed polymers and their melts were assumed to have the density of the corresponding polymer samples at room temperature. The density of the component representing PET decomposition intermediate was assumed to be the mean of the corresponding unpyrolyzed material and final condensed-phase decomposition product densities. Kydex and PEI condensed-phase intermediates were assumed to have the density of the final condensed-phase product. The latter assumption was based on high initial swelling rates observed for these materials in the gasification experiments.

The only remaining undefined parameters in the material pyrolysis models were the thermal conductivities of all condensed-phase components and radiation absorption coefficients of ABS_char, PET_melt, PET_int, Kydex_int, PEI_melt and PEI_int. These parameters were derived from the sample bottom temperatures measured in the gasification experiments conducted at the lowest heat flux. The results of the lowest heat flux experiments were used for parameterization in the current as well as previous (non-charring polymer) study [13] because these experiments were believed to be associated with the most certain and closest to one-dimensional boundary conditions. These temperature data are shown in Figure 9 as points.

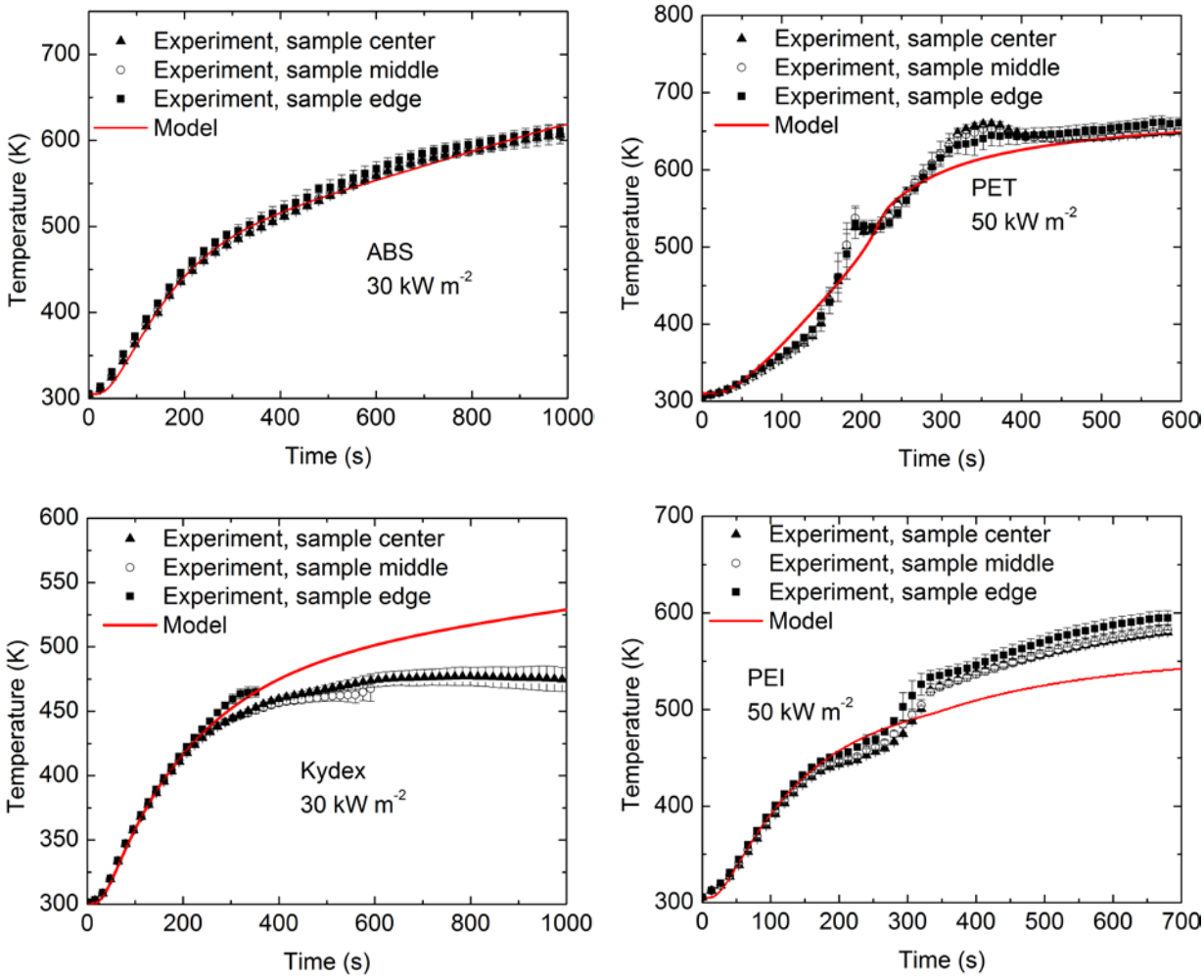

Figure 9. Experimental and simulated bottom surface temperature histories obtained at 30-50 kW m^{-2} of external heat flux.

For ABS and PET, the temperature data collected from different surface locations remain close to each other throughout the experiment further indicating one-dimensional nature of these gasification processes. For PEI, the temperatures start to deviate significantly at around 250 s with the sample center being notably cooler than the edge. In the case of Kydex, the temperatures start to deviate at about the same time. Subsequently, the sample's base gradually retreats from the areas where the edge and middle temperatures are sampled (these areas are defined in Figure 2), which prevents further data collection.

The results of inverse modeling of the bottom surface temperature histories are also shown in Figure 9 (as lines). The thermal conductivity values, which were adjusted together

with the absorption coefficients of the aforementioned components to reproduce the experimental data, are given in Table 4. The thermal conductivities of all condensed-phase components with the exception of those representing the final residues were expressed as a linear function of temperature. The thermal conductivities of the final condensed-phase products were assumed to have an additional third power term, which was used to account for a potential contribution of radiative transport through the radiative diffusion approximation [22]. The uncertainties in the thermal conductivities were estimated by propagating variation in the temperature measurements. Table 4 also summarizes other heat-transfer-related parameters of the condensed-phase components including the radiation absorption coefficients, which are expressed in the concentration-normalized and non-normalized formats.

With the exception of some subtle features of the PET data (such as a small peak at 200 s), the ABS and PET experimental temperature histories are captured well by the corresponding models. For Kydex and PEI, the models capture only the first 300 s of the experiments. No attempt was made to fit the temperature data obtained beyond this point in time because of high uncertainties in the experimental conditions arising from the materials' intumescence.

Table 4. Thermal transport properties of condensed-phase material components.

Component	Density ($kg\ m^{-3}$)	Emissivity	Absorption Coefficient ($m^2\ kg^{-1}$ / m^{-1})	Thermal Conductivity ($W\ m^{-1}\ K^{-1}$)
ABS	1050	0.95	1.71 / 1800	$(0.30\text{-}2.8\times10^{-4}T)$ ±10%
ABS_char	80	0.86	31.3 / 2500	$(0.13\text{-}5.4\times10^{-4}T+4.8\times10^{-9}T^3)$ ±15%
PET	1385	0.95	1.40 / 1940	$(0.35\text{-}4.8\times10^{-4}T)$ ±10%
PET_melt	1385	0.95	1.40 / 1940	$(0.33\text{-}2.0\times10^{-5}T)$ ±15%
PET_int	730	0.95	1.40 / 1020	$(0.45+2.0\times10^{-4}T)$ ±20%
PET_char	80	0.86	100 / 8000	$(0.45+3.8\times10^{-5}T+5\times10^{-10}T^3)$ ±25%
Kydex	1350	0.95	1.58 / 2130	$(0.28\text{-}2.9\times10^{-4}T)$ ±20%
Kydex_int	100	0.95	30.0 / 3000	$(0.55+3.0\times10^{-5}T)$ ±15%
Kydex_char	100	0.86	100 / 10000	$(0.28+8.4\times10^{-5}T+3\times10^{-10}T^3)$ ±25%
PEI	1285	0.95	1.36 / 1750	$(0.40\text{-}4.0\times10^{-4}T)$ ±10%
PEI_melt	1285	0.95	100 / 129000	$(0.32\text{-}3.3\times10^{-4}T)$ ±15%
PEI_int	80	0.95	100 / 8000	$(0.45+1.9\times10^{-4}T)$ ±15%
PEI_char	80	0.86	100 / 8000	$(0.50\text{-}3.4\times10^{-5}T+2\times10^{-10}T^3)$ ±25%

A comparison of the experimental and modeled temperature histories obtained for higher external heat fluxes is shown in Figure 10. Note that these experimental data were not utilized in the heat transport parameterization process. The model of ABS is in a good agreement with all experimental data. The model of PET agrees with the experimental data at the early stages of gasification. At the late stages, the model overpredicts somewhat the experimental bottom surface temperature values. A similar situation is observed for Kydex, although the late stage overprediction by the model is notably more severe. This overprediction (observed for both the low and high heat flux experiments) is expected and can be explained by the Kydex sample's propensity to shift its mass toward the center axis during gasification further insulating the corresponding area of the sample's bottom surface. This phenomenon is not captured by the one-dimensional model.

Unlike the Kydex model, the model of PEI systematically underpredicts the experimental temperatures obtained at higher external heat fluxes. As indicated by the data in Figure 7, PEI samples grow in height notably faster than Kydex samples. They also end up much taller. This behavior is likely to result in the experimental top surface heat fluxes to be underpredicted by the current model (especially in the high heat flux scenarios), which, at least partially, explains the observed temperature discrepancies. The model also does not take into account sample surface oxidation, which may also contribute to the surface heat flow. This oxidation is likely to affect the portion of the sample inside the cone heater, where anaerobic environment cannot be maintained with the present CAPA design.

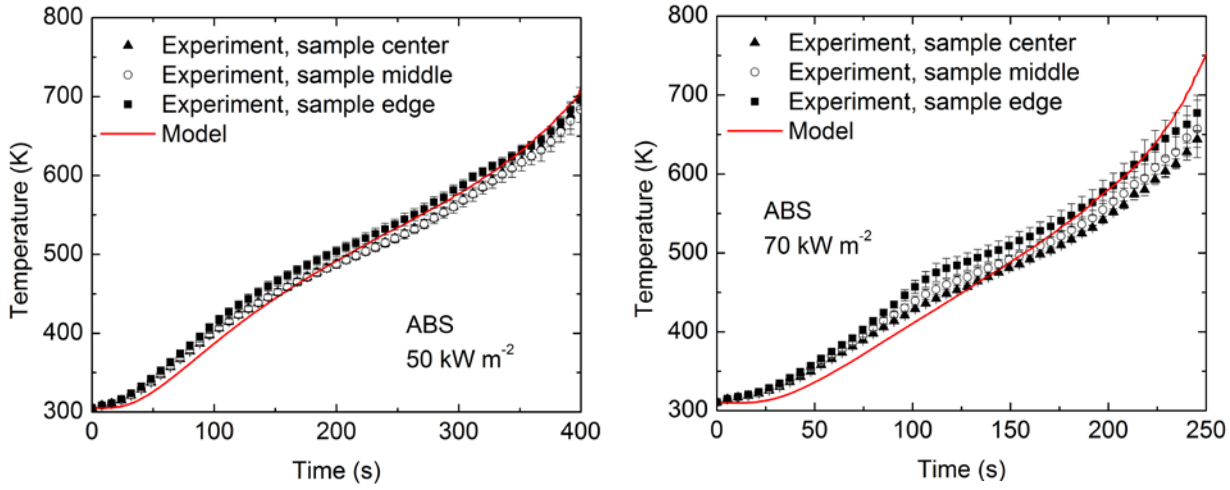

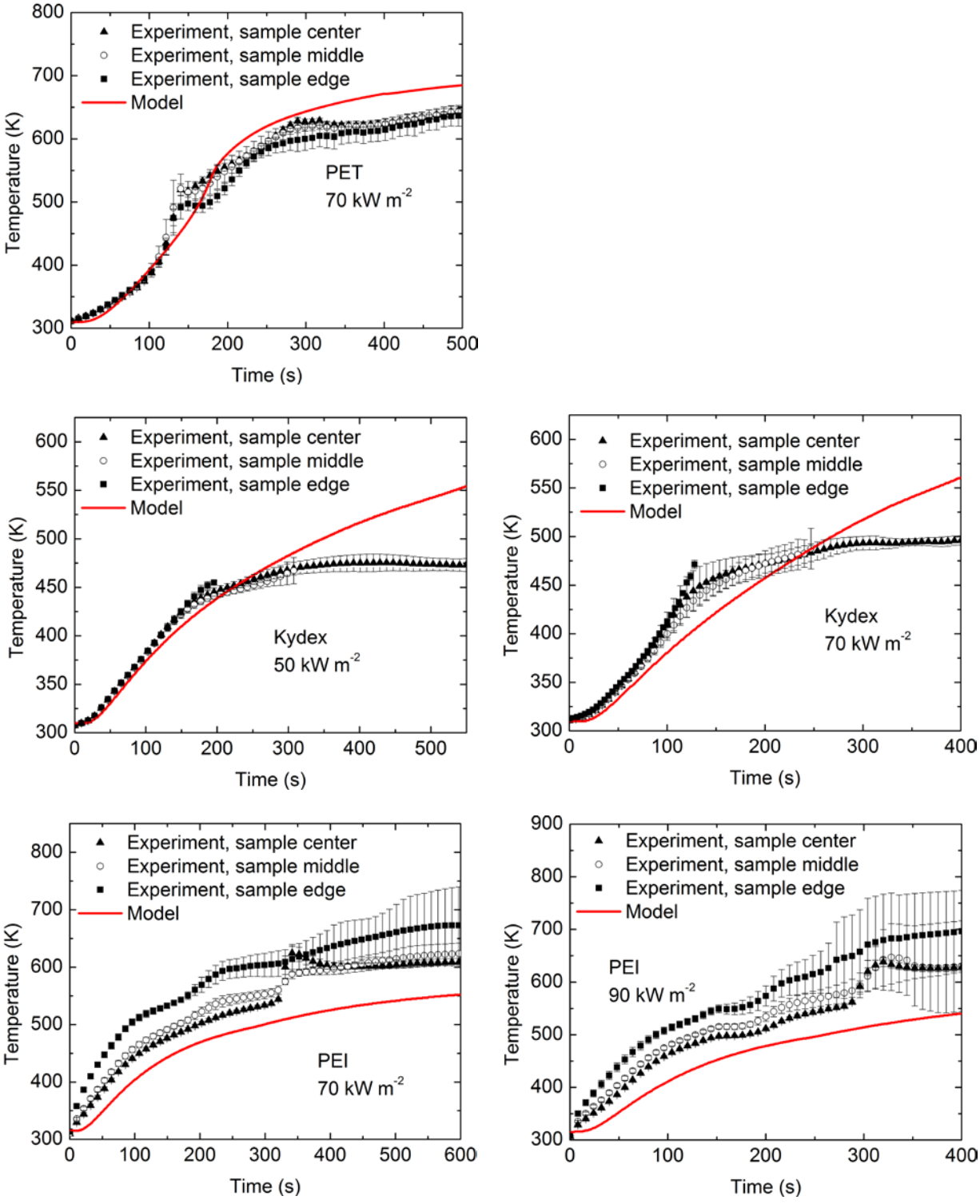

Figure 10. Experimental and simulated bottom surface temperature histories obtained at 50-90 kW m^{-2} of external heat flux.

A comparison of the polymer thermal conductivities obtained in this study to those reported by resin manufacturers or available in the literature is provided in Table 5. Only room temperature values were available from external sources. Assuming that the uncertainties in the literature values are around 15%, the current and literature thermal conductivity ranges overlap for all studied materials with the worst agreement observed for PEI.

Table 5. Comparison of room temperature (300 K) thermal conductivities (W m^{-1} K^{-1}) measured in this study to those reported elsewhere.

Polymer	Current Measurement	Literature Value
ABS	0.22	0.25 [23]
PET	0.21	0.22 [24]
Kydex	0.19	0.16 [25]
PEI	0.28	0.22 [26]

3.4 Mass Loss Rate and Sample Thickness Predictions

A comparison of the mass loss rates measured in the ABS gasification experiments to those predicted by the corresponding model are shown in Figure 11. With the exception of slight overprediction of the 30 kW m^{-2} data at the late stages of gasification, the model performs very well. This agreement indicates validity of the material decomposition kinetics, thermodynamics and heat transfer parameters. All these properties contribute to the definition of the mass loss rate dynamics and its dependence on the external heat flux and none of them were derived from the mass loss rate data.

The mass loss rate predictions obtained for PET are compared with the experimental data in Figure 12. The model slightly underpredicts the middle parts of the experimental curves. These disagreements are probably a consequence of this material's tendency to drip and spatter during pyrolysis. This tendency is also responsible for large uncertainties in the height of the first peak of the experimental curve obtained at 50 kW m^{-2}. Overall, this PET model is a dramatic improvement over an earlier version [27], which was found to underpredict the maximum experimental mass loss rate by more than a factor of 5.

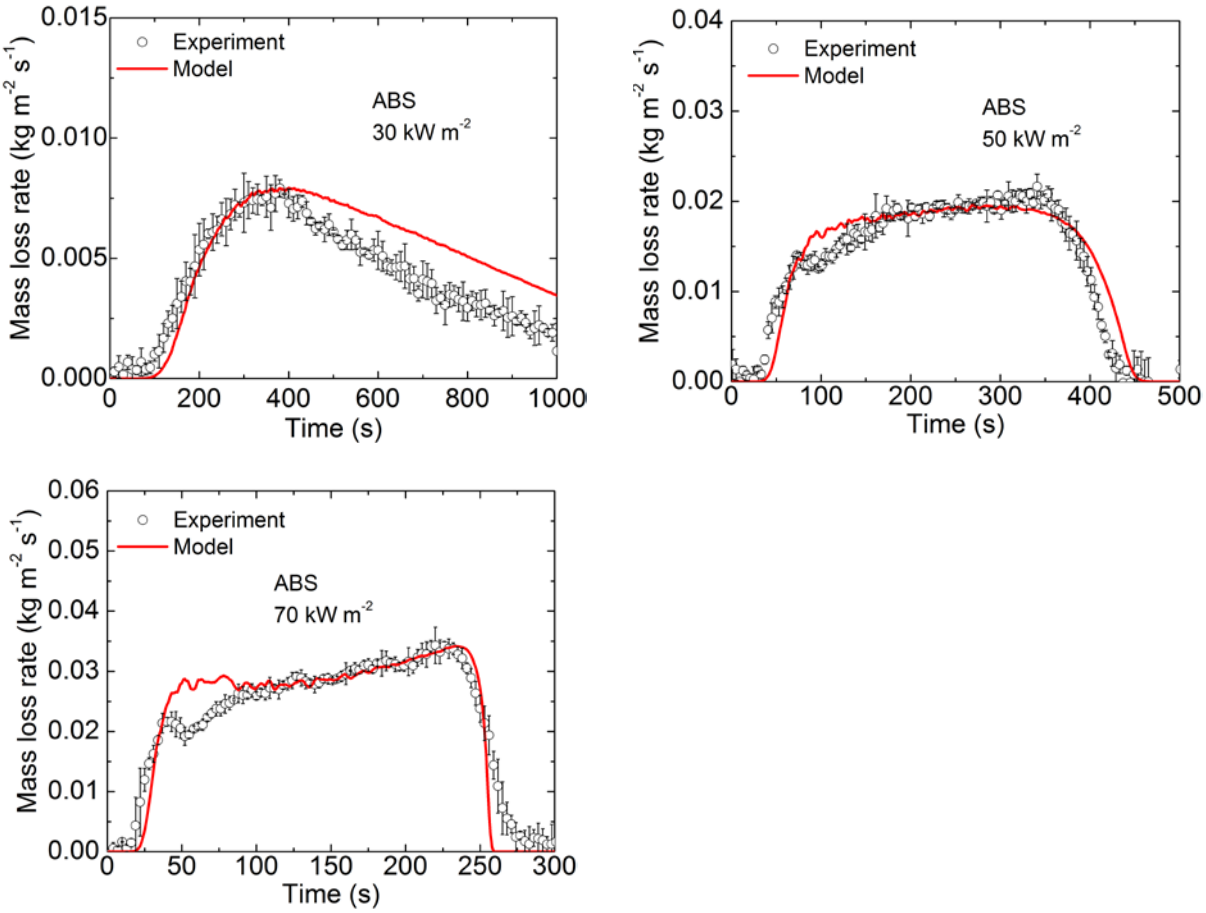

Figure 11. Experimental and simulated mass loss rate histories obtained for ABS at 30-70 kW m^{-2} of external heat flux.

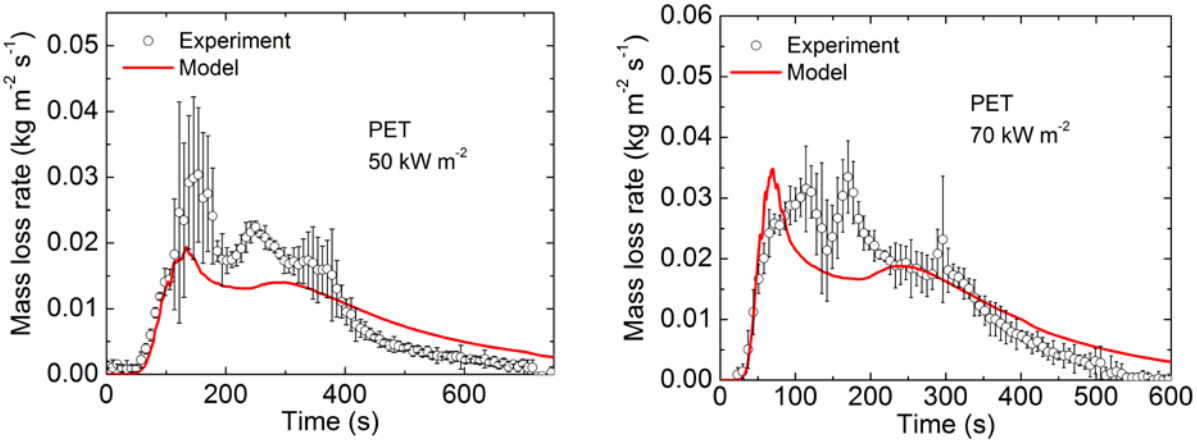

Figure 12. Experimental and simulated mass loss rate histories obtained for PET at 50-70 kW m^{-2} of external heat flux.

Kydex mass loss rate predictions shown in Figure 13 are also in an acceptable agreement with the experimental data, especially taking into account significant deviations of the experimental specimens from the one-dimensional geometry prescribed in the model. Perhaps, the worst agreement between the simulated and experimental mass loss rates was observed for PEI. As indicated in Figure 14, the model systematically underpredicts the experimental mass loss rate at the late stages of gasification. This disagreement is consistent with the discrepancies observed between the experimental and simulated bottom surface temperatures (see Figures 9 and 10) and can be similarly explained by a fast expansion of the PEI samples into the cone heater, which brings increased and difficult-to-characterize surface heating and oxidation.

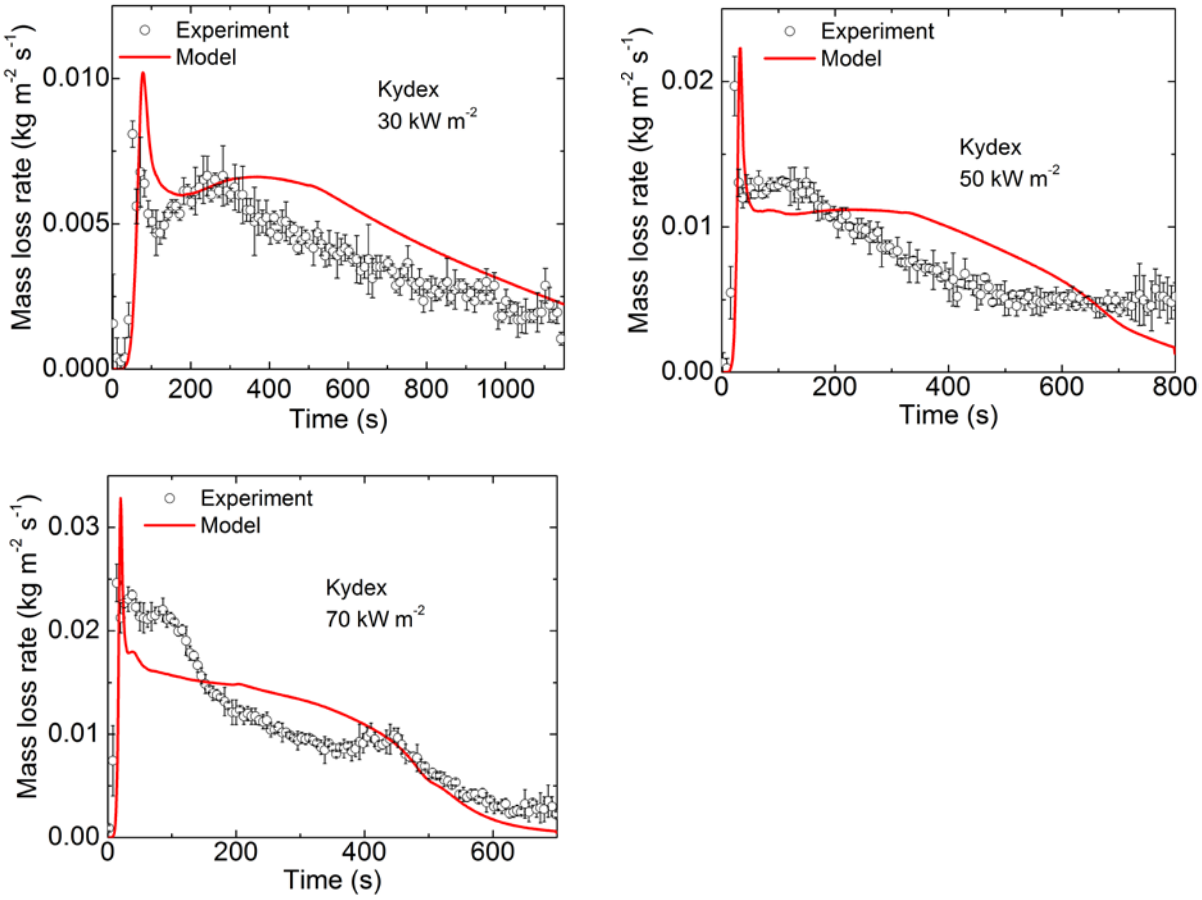

Figure 13. Experimental and simulated mass loss rate histories obtained for Kydex at 30-70 kW m^{-2} of external heat flux.

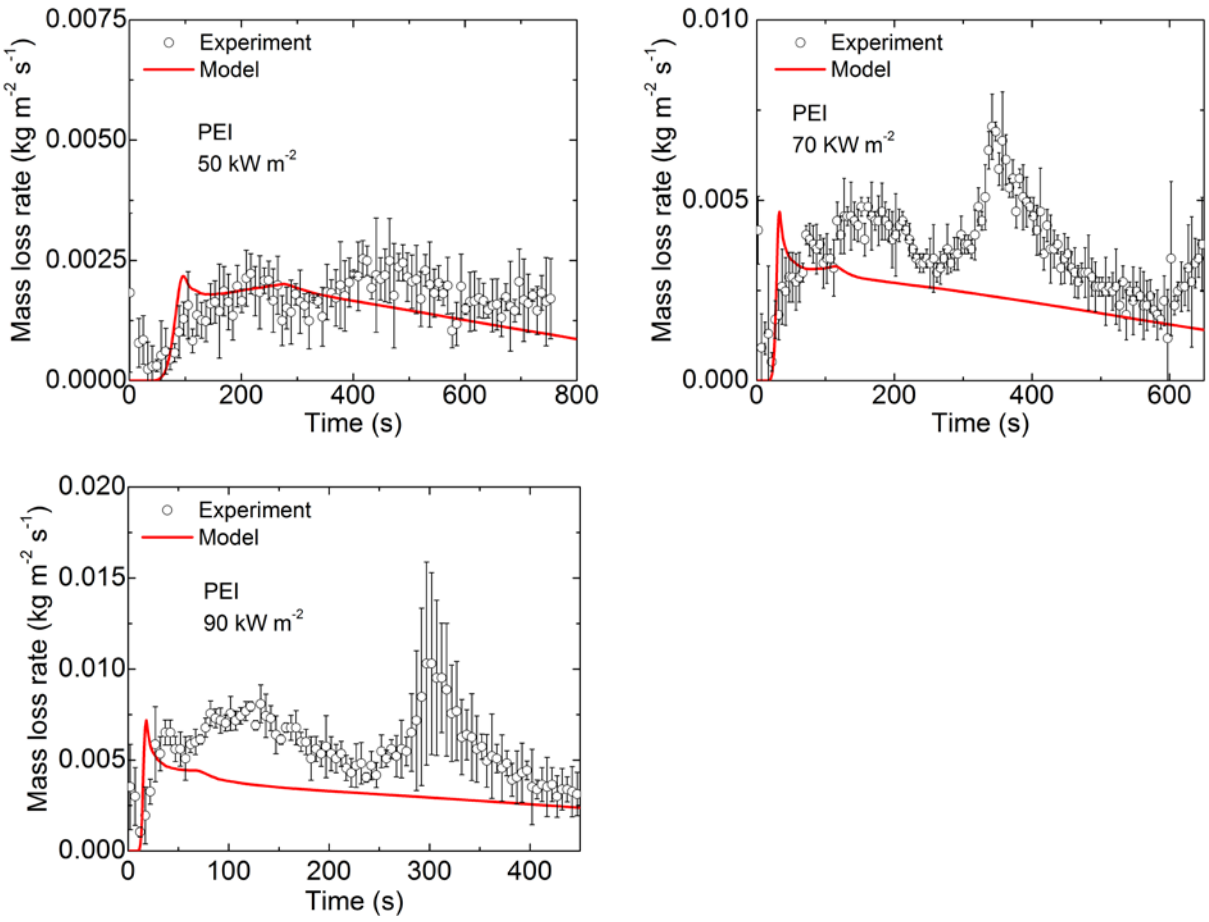

Figure 14. Experimental and simulated mass loss rate histories obtained for PEI at 50-90 kW m^{-2} of external heat flux.

Finally, the ability of the models to predict intumescence of the charring polymers was examined. A comparison between the experimental and simulated sample thickness dynamics obtained at 50 kW m^{-2} is shown in Figure 15. ABS was excluded from this comparison because its samples, while producing a char layer, did not demonstrate intumescent behavior. For the gasification of PET and early stages of gasification of Kydex, the agreement is reasonable, taking into account that the experimental data on both polymers represent the maximum sample thickness (as explained in Subsection 3.2). For the gasification of PEI and late stages of gasification of Kydex, the agreement is rather poor: the models considerably underestimate the sample thicknesses. Non-one-dimensional swelling of these samples accounts for the main

portion of these discrepancies. However, notable early disagreements in the PEI data suggest that other factors, such as potentially significant dependence of the material's density on temperature (which is not included in the current models), may have also contributed to the observed differences.

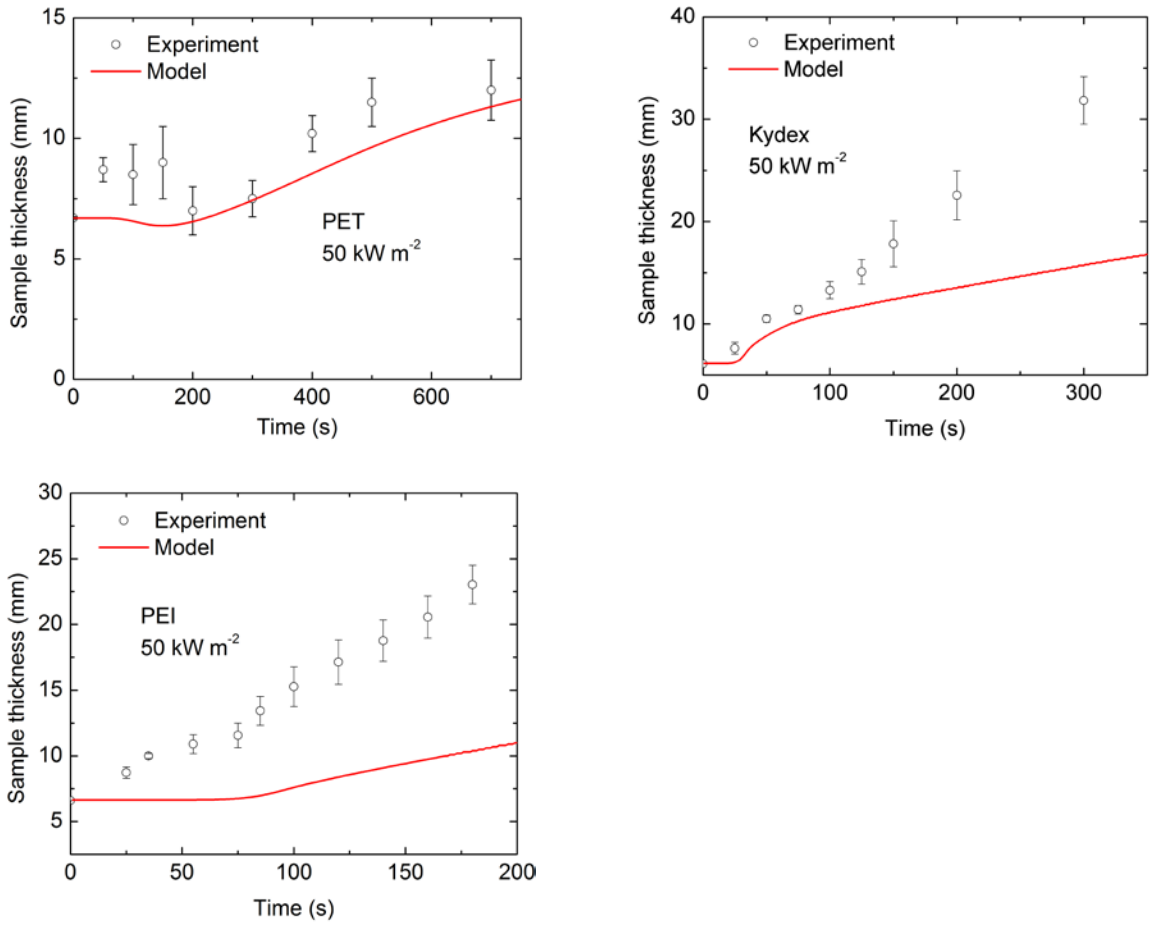

Figure 15. A comparison between experimental and simulated sample thickness histories obtained at 50 kW m^{-2} of external heat flux.

4. Conclusions

Controlled atmosphere gasification experiments including simultaneous mass loss monitoring and spatially-resolved thermometry were combined with broadband radiation absorption measurements and inverse pyrolysis modeling to parameterize heat transfer in several

polymers exhibiting a wide range of charring behaviors. Previously performed thermogravimetric analysis and differential scanning calorimetry [8-9], which were used to determine the kinetics and thermodynamics of the thermal decomposition of these materials, provided a foundation for the pyrolysis models. Overall, this approach was found to produce property sets that demonstrated satisfactory predictions of the mass loss (or burning) rates over a wide range of heating conditions simulating fire exposure.

This study also revealed notable limitations of the gasification experiment and the one-dimensional modeling framework when applied to highly intumescent solids (such as Kydex and PEI). These limitations are thought to be the main reason for the observed disagreements between the results of modeling and experiments. Substantial sample swelling during the gasification produced large heating intensity and atmosphere composition uncertainties, which made it impossible to rely on a significant portion of the data either for the model parameterization or validation. Improving this experiment to extend the time during which well-characterized conditions are maintained for highly intumescent materials will be a subject of future work.

The intumescence also manifested itself in substantial deviations from near one-dimensional initial sample geometry, despite the fact that a concerted effort was made to minimize any spatial non-uniformity in the initial heating conditions. It is clear that a higher dimensionality pyrolysis model will be required to fully capture the heat transfer and swelling dynamics of highly intumescent coupon-sized samples. It may also be necessary to include at least some solid mechanics and related edge effects into this model to correctly represent all intumescence-related processes and to enable a meaningful extrapolation of the observed behavior to larger specimens.

Acknowledgements

This work was partially supported by the NIST grant #60NANB10D0226. The authors would like to thank the grant monitor, Dr. Kevin B. McGrattan, for helpful discussions.

References

1. Bourbigot S., Duquesne S., "Fire Retardant Polymers: Recent Developments and Opportunities," *Journal of Materials Chemistry,* vol. 17, pp. 2283-2300 (2007).

2. Quintiere J. G., *Fundamentals of Fire Phenomena,* John Wiley & Sons, Chichester, UK, 2006.

3. Atreya A., "Pyrolysis of Wood," Ph.D. Dissertation, Harvard University, Cambridge, MA, 1983.

4. Di Blasi C., "Analysis of Convection and Secondary Reaction Effects Within Porous Solid Fuels Undergoing Pyrolysis," *Combustion Science and Technology,* vol. 90, pp. 315-340 (1993).

5. Moghtaderi B., Novozhilov V., Fletcher D., Kent J. H., "An Integral Model for the Transient Pyrolysis of Solid Materials," *Fire and Materials,* vol. 21, pp. 7-16 (1997).

6. Staggs J. E. J., "Heat and Mass Transport in Developing Chars," *Polymer Degradation and Stability,* vol. 82, pp. 297-307 (2003).

7. Delichatsios M., Paroz B., Bhargava A., "Flammability Properties for Charring Materials," *Fire Safety Journal,* vol. 38, pp. 219-228 (2003).

8. Li J., Stoliarov S. I., "Measurement of Kinetics and Thermodynamics of the Thermal Degradation for Non-charring Polymers," *Combustion and Flame*, vol. 160, pp. 1287-1297 (2013).

9. Li J., Stoliarov S. I., "Measurement of Kinetics and Thermodynamics of the Thermal Degradation for Charring Polymers," *Polymer Degradation and Stability,* vol. 106, pp. 2-15 (2014).

10. Stoliarov S. I., Lyon R. E., "Thermo-Kinetic Model of Burning," Federal Aviation Administration Technical Note, DOT/FAA/AR-TN08/17 (2008).

11. Lautenberger C., Fernandez-Pello C., "Generalized Pyrolysis Model for Combustible Solids," *Fire Safety Journal,* vol. 44, pp. 819-839 (2009).

12. McGrattan K., Hostikka S., McDermott R., Floyd J., Weinschenk C., Overholt K., "Fire Dynamics Simulator (Version 6) Technical Reference Guide," National Institute of Standards and Technology Special Publication 1018-6 (2014).

13. Li J., Gong J., Stoliarov S. I., “Gasification Experiments for Pyrolysis Model Parameterization and Validation,” *International Journal of Heat and Mass Transfer,* vol. 77, pp. 738-744 (2014).

14. ASTM Standard E1354 - 13, Standard Test Method for Heat and Visible Smoke Release Rates for Materials and Products Using an Oxygen Consumption Calorimeter, ASTM International, West Conshohocken, PA (2013).

15. Semmes M., Liu X., McKinnon M. B., Stoliarov S. I., Witkowski A., "A Model for Oxidative Pyrolysis for Corrugated Cardboard," *Proceedings of the Eleventh International Symposium on Fire Safety Science* (2014).

16. Li J., “A Multiscale Approach to Parameterization of Burning Models for Polymeric Materials,” Ph.D. Dissertation, University of Maryland, College Park, MD, 2014.

17. Linteris G., Zammarano M., Wilthan B., Hanssen L., "Absorption and Reflection of Infrared Radiation by Polymers in Fire-like Environments," *Fire and Materials,* vol. 36, pp. 537-553 (2012).

18. Tsilingiris P. T., “Comparative Evaluation of the Infrared Transmission of Polymer Films,” *Energy Conversion and Management,* vol. 44, pp. 2839-2856 (2003).

19. Stoliarov S. I., Leventon I. T., Lyon R. E., “Two-dimensional Model of Burning for Pyrolyzable Solids,” *Fire and Materials,* vol. 38, pp. 391-408 (2014).

20. NIST Chemistry WebBook, The National Institute of Standards and Technology (NIST) Standard Reference Database 69. Available at webbook.nist.gov/chemistry/

21. Matsumoto T., Ono A., "Specific Heat Capacity and Emissivity Measurements of Ribbon-shaped Graphite using Pulse Current Heating," *International Journal of Thermophysics,* vol. 16, pp. 267-275 (1995).

22. Siegel R., Howell J., *Thermal Radiation Heat Transfer,* Taylor & Francis, New York, 2002.

23. SubsTech (2014, Dec. 2), *Thermoplastic Acrylonitrile-Butadiene-Styrene (ABS).* Available at www.substech.com/dokuwiki/doku.php?id=thermoplastic_acrylonitrile-butadiene-styrene_abs

24. Van Krevelen D. W., te Nijenhuis K., *Properties of Polymers: Their Correlation with Chemical Structure; Their Numerical Estimation and Prediction from Additive Group Contributions*, Elsevier, Oxford, UK, 2009.

25. SEKISUI America Corporation (2014, Dec. 2), *Kydex Physical Properties*. Available at www.kydex.com/technical-data/FAQs.aspx

26. SABIC (2014, Dec. 2), *ULTEM Resin 1000*. Available at www.sabic-ip.com/gepapp/eng/weather/weatherpdf?sltRegionList=1002002000&sltPrd=1002003018&sltGrd=1002011252&sltUnit=Metric&sltSSO=0&sltLDAP=0&sltType=PDF&sltVersion=Internet&sltModule=DATASHEETS

27. Linteris G. T., Lyon R. E., Stoliarov S. I., "Prediction of the Gasification Rate of Thermoplastic Polymers in Fire-like Environments," *Fire Safety Journal,* vol. 60, pp. 14-24 (2013).